

Diffusion Model-based Parameter Estimation in Dynamic Power Systems

Feiqin Zhu^{1†}, Dmitrii Torbunov^{2†}, Zhongjing Jiang^{3,4},
Tianqiao Zhao¹, Amirthagunaraj Yogarathnam¹, Yihui Ren^{2*},
Meng Yue¹

¹Interdisciplinary Science Department, Brookhaven National Laboratory,
Upton, 11973-5000, NY, USA.

^{2*}Computing and Data Sciences Directorate, Brookhaven National
Laboratory, Upton, 11973-5000, NY, USA.

³Environmental and Climate Sciences Department, Brookhaven National
Laboratory, Upton, 11973-5000, NY, USA.

⁴Institute for Sustainability, Energy, and Environment, University of
Illinois Urbana-Champaign, Urbana, 61801, IL, USA.

*Corresponding author(s). E-mail(s): yren@bnl.gov;
Contributing authors: hzfq@outlook.com; dtorbunov@bnl.gov;
zjiang35@illinois.edu; tzhao1@bnl.gov; rajyogar@ieee.org;
yuemeng@bnl.gov;

[†]These authors contributed equally to this work.

Abstract

Parameter estimation, which represents a classical inverse problem, is often ill-posed as different parameter combinations can yield identical outputs. This non-uniqueness poses a critical barrier to accurate and unique identification. This work introduces a novel parameter estimation framework to address such limits: the Joint Conditional Diffusion Model-based Inverse Problem Solver (JCIDI). By leveraging the stochasticity of diffusion models, JCIDI produces possible solutions revealing underlying distributions. Joint conditioning on multiple observations further narrows the posterior distributions of non-identifiable parameters. For the challenging task in dynamic power systems: composite load model parameterization, JCIDI achieves a 58.6% reduction in parameter estimation error compared to the single-condition model. It also accurately replicates system's dynamic responses under various electrical faults, with root mean square errors below 4×10^{-3} , outperforming existing deep-reinforcement-learning and supervised

learning approaches. Given its data-driven nature, JCDI provides a universal framework for parameter estimation while effectively mitigating the non-uniqueness challenge across scientific domains.

Keywords: Composite load model, Diffusion model, Dynamic power system, Inverse problem, Joint condition, Parameter non-uniqueness

1 Introduction

Dynamical system modeling is fundamental across many scientific disciplines, from synoptic meteorology to electric power grids. While forward modeling, which predicts system evolution from initial states, has received extensive attention, many practical problems in system dynamics, such as parameter identification, are framed as inverse problems, where inherent properties are deduced from observed behaviors [1]. For systems with complex dynamics, such inference becomes particularly challenging due to the non-uniqueness of solutions, which is also referred to as *parameter non-identifiability*, where multiple parameter sets can produce identical system behaviors [1, 2].

The modern power system presents a compelling case for studying the inverse problem in system dynamics. Driven by clean energy initiatives, electric power grids are undergoing unprecedented transformation through the widespread integration of renewable energy generation, as well as emerging electrical loads such as electric vehicles and grid-interactive buildings [3–5]. This evolution has dramatically increased the complexity and uncertainty of power system dynamics. Electrical loads, constituting a fundamental component of power systems, are characterized by their numerous quantities, spatial dispersion, and heterogeneity [6]. Accurate load modeling is crucial for analyzing contingencies and stability in large-scale power systems while presenting unique challenges [7]. Load aggregation addresses this challenge by consolidating various individual power loads into an equivalent model, reducing computational complexity yet preserving essential behavioral characteristics. The composite load model (CLM) represents a class of component-based aggregated models that categorizes individual end user load devices into several component groups based on their electrical characteristics [8]. Nevertheless, the CLM operates as a gray box model with specified structure but unknown parameters.

The proliferation of grid sensing devices, such as phasor measurement units (PMUs), provides extensive measurement data that capture the dynamic behaviors of electric loads under various disturbances. The parameterization of CLM from these measurements exemplifies a classical inverse problem (Fig. 1). Despite significant simplifications from detailed load representations, CLM still encompasses dozens of differential algebraic equations with almost 200 parameters to be determined. The inverse problem of parameterization for such a complex, nonlinear dynamical system is usually ill-posed – the solution may not be unique, and minor input variations can produce dramatic changes of output, yielding unstable results [9–11]. This non-uniqueness of parameter

estimates limits generalization across different dynamic disturbances, i.e., CLM parameters carefully selected under one electrical fault-induced disturbance may exhibit inadequate performance in another fault.

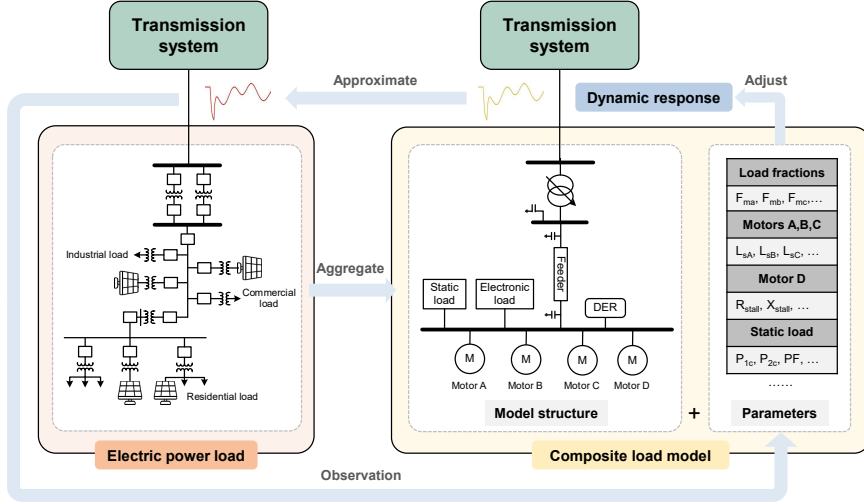


Fig. 1 Parameterization for the composite load model. CLM uses several types of load devices to represent the aggregation behavior of the numerous power loads. The parameterization of CLM represents a classical inverse problem, which deduces model parameters from the observed dynamic responses. With the estimated parameters, CLM is expected to approximate its dynamic behavior to real measurements.

Data-driven machine learning (ML) has emerged as a promising paradigm for modeling complex system dynamics [12–14]. Recent advances, such as the physics-informed neural network (PINN) and conditional generative adversarial networks (cGANs), are demonstrated to provide more accurate and efficient solutions for both forward and inverse problems [15–17]. In the context of CLM parameterization, reinforcement learning (RL) has been extensively investigated [18–20]. It reformulates parameter calibration as a Markov decision process (MDP) wherein policies are learned to adjust model parameters toward minimal observation error through trial and error. However, it tends to fall into local optimum, especially when the action space is large. Additionally, RL requires iterative reevaluation with forward simulation for each trial of new model parameters, which becomes computationally expensive when the grid simulation model is complex. Supervised learning (SL) neural networks, such as the multi-residual deep learning structure proposed in [21], present an alternative approach. They extract the observation features and directly learn the mapping between observations and model parameters. These networks, however, often fail to represent the one-to-many mapping between observations and parameters [22]. Recent advances in probabilistic approaches include deep generative architectures for time-varying parameter identification [23] and amortized Bayesian estimation using conditional masked autoregressive flow [24]. While these methods effectively manage uncertainty, they do not address

the parameter non-uniqueness problem. Recent RL investigations have explored multi-event training and multi-task learning strategies to cope with this challenge [25, 26]. However, non-stationarity in multi-event environments can degrade the performance of learning agents, and multi-task learning risks negative transfer between tasks.

As an emerging new family of deep generative models, diffusion models construct synthetic data samples by gradually adding random noise to data then learning to reverse the diffusion process [27]. The model faithfully learns the probability distribution of a dataset and provides a means to generate new samples from this distribution. It has achieved state-of-the-art generation quality compared with existing generative models, such as GANs [28–31]. Diffusion models also can be trained in a conditioned form, allowing flexible control over the generation process toward the expected style. Along with forward generation, the denoising technology represents a compelling approach for solving inverse problems by implicitly encoding valuable information from input signals [32]. Diffusion-model-based solutions have been successfully developed for a variety of inverse problems, such as image restoration and super-resolution [33]. However, none of the current work involves the inverse problem applied in dynamical systems, such as parameter estimation.

Here, we present a novel probabilistic parameter estimation framework based on the generative diffusion model, named *Joint Conditional Diffusion Model-based Inverse Problem Solver* (JCIDI), as depicted in Figure 2. In this framework, we train the conditional diffusion model to learn the inherent distributions within parameter space and provide a data-driven solution for parameter estimation. The key innovations of this work include:

1. Distinct from traditional conditioning mechanisms, where diffusion models rely on labeled conditions, we condition the diffusion model on system observations and generate system parameters that are constrained by the observations.
2. The probabilistic nature of diffusion models enables them to produce a distribution of parameters consistent with the observations, allowing for studying the parameter correlations and quantifying uncertainties.
3. We develop a novel denoising neural network architecture based on a transformer encoder. It processes model parameters as input tokens and uses its attention mechanism to learn parameter correlations, as well as the relationships between these parameters and their corresponding observations.
4. To address the parameter non-uniqueness problem, we introduce the multi-event joint conditioning mechanism: *conditioning the diffusion model on multiple observations under various disturbances*. It produces a posterior parameter distribution that satisfies various observation constraints simultaneously. This joint conditional probability effectively reduces parameter estimation uncertainties.

With the study of CLM in power systems, we demonstrate a significant improvement of 58.6% in parameter estimation accuracy with the increase of conditioned fault events. Compared with the existing RL- and SL-based methods, JCIDI achieves the most precise prediction of system responses under various fault events, without requiring repeated simulations. Beyond power system modeling, this approach can be extended to mitigate the parameter non-uniqueness challenge in diverse dynamical systems, leveraging its data-driven nature, and probabilistic inference with the ability to handle

multiple conditional observations. This generality, along with substantial improvements over existing methods, suggests that JCIDI could become a valuable tool for solving complex parameter identification problems across scientific disciplines.

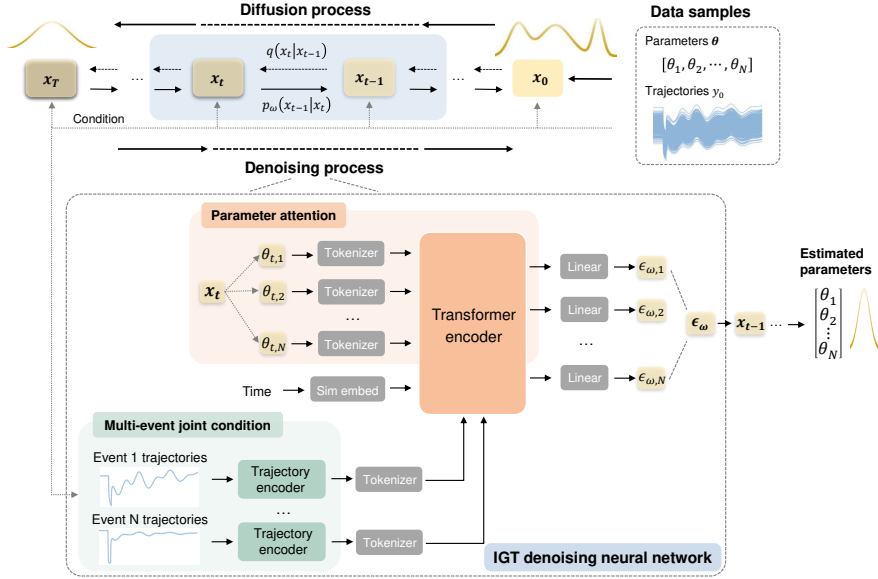


Fig. 2 Illustration of JCIDI Framework. This framework is based on a conditional diffusion model. The diffusion and reverse processes are applied on the model parameter space. Systems observations serve as the conditions to guide the generation process. The denoising neural network is constructed based on a transformer encoder. Three types of inputs—1) model parameters, 2) encoded power trajectories, and 3) encoded diffusion time step—are tokenized and fed into the neural network. The multi-event joint conditioning mechanism is employed, enabling the diffusion model to be simultaneously conditioned on multiple observations under various dynamic disturbances.

2 Results

Simulation settings. We adopt the advanced CLM – composite load model with distributed generation (CMPLDWG) [34] developed by Western Electricity Coordinating Council (WECC). This state-of-the-art model incorporates the increasingly penetrated power electronic-interfaced loads, single-phase induction motors (IMs), and distributed energy resources (DERs). The CMPLDWG model details are illustrated in Supplementary Section 1. By applying electrical fault-induced disturbances in the transmission system, we generate the dynamic responses of CMPLDWG, including the transient trajectories of active and reactive powers measured at the interconnection point. Specifically, three distinct electrical faults with different fault clearing times and bus locations (Supplementary Section 4 are selected for the simulation study, including one that results in power electronic load tripping (*trip fault*), one which induces motor D stalling (*stall fault*), and another that exhibits neither phenomenon (*ordinary fault*).

CMPLDWG contains nearly 200 parameters. Some demonstrate significant impact on the system dynamics, while others have minor effects and are difficult to estimate. To solve the parameterization problem efficiently and effectively, we conduct global sensitivity analysis using Sobol’s method. The analysis details and key findings are presented in Supplementary Section 3 , which reveal notable sensitivity variations across different fault events. Based on the parameter rankings according to the total Sobol indices under various fault events (Supplementary Fig. 6), we select 30 parameters with relatively high sensitivity for identification. Supplementary Table 2 lists these parameters along with their notations and physical meanings. We generate training and testing datasets by perturbing these sensitive parameters and running grid simulations under different fault-induced disturbances. Supplementary Section 4 provides details of the data generation process.

Parameter estimation uncertainties. We train our diffusion model-based parameterization framework to estimate system parameters from observed dynamic responses under grid fault-induced disturbances. The algorithm implementation details are explained in Supplementary Section 4 . To evaluate the effectiveness of multi-event joint conditioning, we compare JCDDI conditioned on three fault events, including ordinary, trip, and stall faults, with CDI (Conditional Diffusion Model-based Inverse Problem Solver) conditioned solely on the ordinary fault.

We inject the desired power trajectories into the well-trained diffusion models and deduce the posterior results of parameter estimation (Supplementary Fig. 8). Some representative cases are displayed in Fig. 3. One thousand samples of parameter estimates are generated given the desired power trajectories, which are simulated with the default model parameters featured in Supplementary Table 2 .

Parameter non-identifiability can arise due to several reasons: 1) Some parameters may have vanishingly low sensitivity under specific conditions, making them practically unidentifiable from the available data; 2) Some model parameters exhibit complex dependencies on each other. Then, different combinations of parameters that satisfy a specific mathematical relation can yield identical model outputs [35]. We use mutual information (MI) to quantitatively evaluate parameter dependencies [36, 37]. MI quantifies how much information one random variable provides about another. It can be calculated by Kullback–Leibler (KL) divergence between the joint distribution and the product of the marginal distributions of the two variables, as expressed by (1) [38, 39]. We present the calculation results in Fig. 3.

$$I(X;Y) = \int_y \int_x p(x,y) \log \left(\frac{p(x,y)}{p(x)p(y)} \right) dx dy \quad (1)$$

where $p(x,y)$ is the joint probability density function of X and Y , $p(x)$ and $p(y)$ respectively represent the marginal probability density functions of X and Y .

Our findings reveal significant correlations among several sets of model parameters estimated by CDI. The load fractions F_{mb} and F_{mc} , F_{md} and F_{el} are negatively correlated, yielding high MIs greater than 1 nat. The power factor of motor D ($CompPF$) and the initial reactive power of electronic load (Q_{el0}) exhibit positive correlation, with an MI of 0.837 nat. In addition, we also observe notable correlations between

parameter pairs (F_{mb} and L_{sA}) and (F_{mc} and L_{sA}), showing MI values above 0.5 nat. These parameter combinations yield similar post-fault trajectories, validating their non-identifiability due to interdependency. Theoretically, these correlations can be attributed to the counteracting contributions of steady states or dynamic behaviors associated with different load components, i.e., varied combinations of parameters may have opposite effects on the dynamic responses of individual loads, preserving the invariance of the total system response. However, the MI between R_{stall} and X_{stall} is merely 0.001 nat, indicating no statistical correlation. CDI fails to identify R_{stall} and X_{stall} because they exhibit negligible sensitivity under the ordinary fault event (Supplementary Fig. 6), where motor D stall does not occur.

When comparing JCDI with CDI, we find JCDI produces more concentrated posterior distributions with reduced variance for these non-identifiable model parameters. For the correlated parameters, we notice their MIs are significantly reduced when estimated by JCDI. This implies JCDI effectively mitigates the parameter non-identifiability, as it introduces more constraints under different fault conditions. As a result, F_{md} , F_{el} , Q_{el0} , and $CompPF$ estimated by JCDI closely approximate the true values. For the insensitive parameters, they exhibit significantly enhanced sensitivity under the additional faults, with the occurrence of motor D stalling and electronic load tripping. The enhanced sensitivity facilitates their identification. Therefore, JCDI significantly narrows the posterior distributions of model parameters that fail to be estimated by CDI, such as R_{stall} , X_{stall} , f_{rcel} , N_{q1} , and N_{q2} . It's also interesting to note that R_{stall} and X_{stall} present a significant positive correlation with a high MI of 2.59 nat when estimated by JCDI. This correlation appears with the occurrence of motor D stalling. More constraints would be required for mitigation.

When evaluating parameter estimation accuracy, mean absolute percentage error (MAPE) is commonly used to measure relative precision [40]. However, it becomes invalid when the actual parameter value equals zero. To address this limitation, we define range percentage error (RPE) for individual model parameter as formulated in equations (2). We then use mean absolute range percentage error (MARPE), the average of RPEs across different model parameters, to assess the overall estimation accuracy. In both RPE and MARPE calculations, the absolute parameter errors are normalized by the parameter ranges rather than the actual parameter values, ensuring valid and consistent measurements across all parameter values—regardless of their positions within the specified range.

$$RPE_i = 100 \left| \frac{\hat{\theta}_i - \theta_{i,0}}{UB_i - LB_i} \right|, \quad (2)$$

where $\hat{\theta}$ and θ_0 respectively represent the estimated and actual values of parameters, UB and LB denote the upper and lower bounds, and i is the parameter index.

Figure 4 presents the calculation result of RPE. Some of the model parameters, e.g., F_{md} , F_{el} , f_{rcel} , and Q_{el0} , exhibit high uncertainties when estimated by CDI. The mean MARPE across all parameter estimate samples is 18.0%. Nevertheless, JCDI significantly reduces the estimation errors for multiple model parameters, particularly for those that present higher sensitivity under the trip and stall faults, such as F_{el} , F_{md} , f_{rcel} , R_{stall} , X_{stall} , and F_{rst} , as well as the correlated parameters, including F_{mb} ,

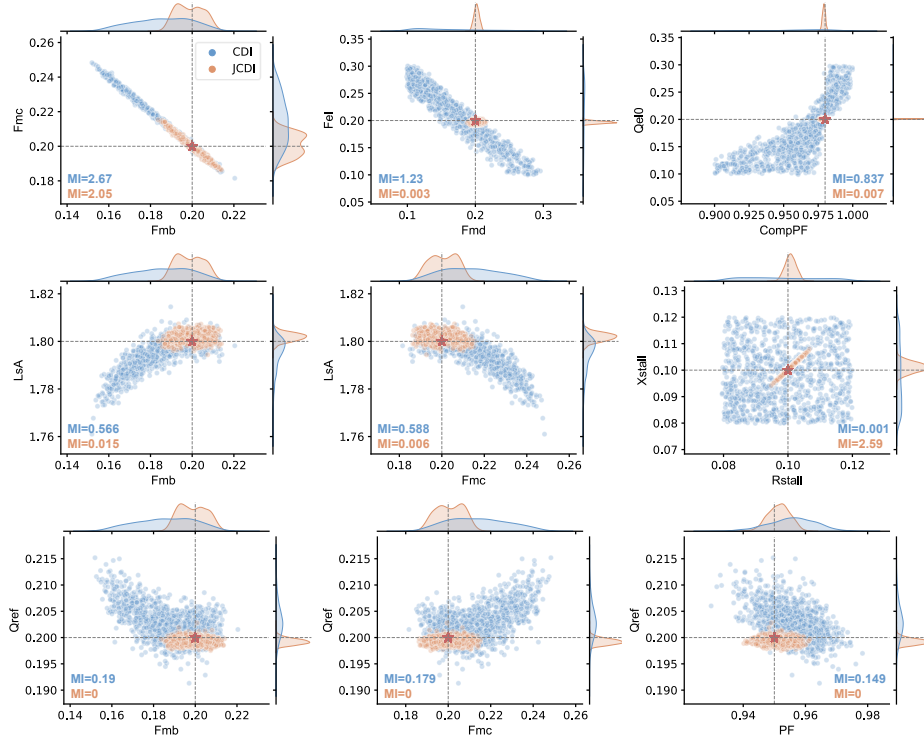


Fig. 3 Representative cases of parameter posterior results. The scatter plots reveal correlations among parameter pairs. The marginal distribution for each model parameter is displayed along the top and right edges, demonstrating JCDD produces more concentrated posterior distributions for the non-identifiable parameters. Blue and orange dots represent parameters estimated by CDI and JCDD, respectively, with pink stars indicating the actual values. The statistical figures are constructed with 1000 data samples.

F_{mc} , Q_{el0} , and $CompPF$. As a result, the mean MARPE decreases to 7.46%. Together, these findings suggest that with multi-event joint conditioning, JCDD effectively reduces the parameter uncertainties, yielding more accurate parameter estimates.

Prediction of dynamic responses. Next, we analyze the replication results of dynamic responses with the estimated model parameters. Substituting the estimated model parameters into CMPLDWG, we perform transient simulations under different fault-induced disturbances, with the resulting power trajectories shown in Fig. 5a. To assess prediction accuracy, we calculate the root mean squared error (RMSE) between the simulated and actual power trajectories as formulated in equation (3). Figure 5b shows the RMSE results.

$$RMSE = \sqrt{\sum_{t=1}^T \frac{(p_{\hat{\theta}}(t) - p_0(t))^2}{T}} + \sqrt{\sum_{t=1}^T \frac{(q_{\hat{\theta}}(t) - q_0(t))^2}{T}}, \quad (3)$$

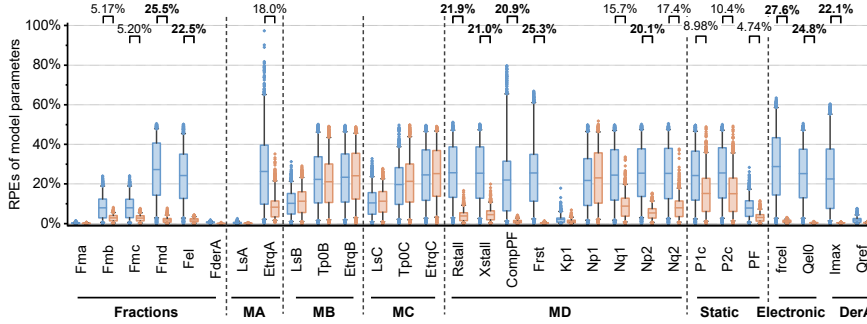


Fig. 4 Range percentage errors of estimated model parameters. Range percentage errors are calculated using equation (2) for each model parameter across 1000 data samples and visualized through the box plot. The boxes cover the intervals from the 25th to 75th percentiles with mean values shown as horizontal lines. The lower and upper ends of the whiskers respectively represent the 5th and 95th percentiles, while the dots beyond these bounds indicate the outliers.

where $p_{\hat{\theta}}(t)$ and $q_{\hat{\theta}}(t)$ respectively represent the estimated active and reactive powers at time t , $p_0(t)$ and $q_0(t)$ are the actual active and reactive powers, and t is the time instant.

As a form of data regularization, we initiate the electrical faults at a common time of 0.5 s from the system’s steady states. Therefore, the power trajectories well encompass the pre-fault steady-state conditions, the transient responses during the faults, and the post-fault dynamic recovery processes. When the electric faults occur, both active and reactive powers dip significantly. For the ordinary fault event, the powers oscillate dynamically and recover to their initial values after fault clearance. However, the steady-state powers settle below the initial value due to incomplete load recovery with electronic load tripping, and the absolute values of steady powers increase significantly after the fault with motor D stalling. Despite parameter estimation uncertainties, both CDI and JCDI accurately predict power trajectories for the ordinary fault, achieving mean RMSEs of approximately 1×10^{-3} . Nevertheless, we observe substantial deviation between the power trajectories predicted by CDI and the actual ones for the trip and stall faults with the mean RMSEs increasing to 4.44×10^{-2} and 7.97×10^{-1} , respectively. In contrast, JCDI maintains high prediction accuracy for these two faults with respective mean RMSEs of 8.61×10^{-4} and 3.75×10^{-3} . These results reveal the limitations of parameter estimation using a single disturbance, where some solutions fail to replicate system dynamic behavior under additional disturbances. Importantly, JCDI achieves consistent performance across different fault-induced disturbances by successfully constraining the non-identifiable parameters.

Out-of-distribution generalization evaluation. While the model parameters are derived from observed dynamic responses under specific fault-induced disturbances during training, they are also expected to accurately predict responses under unencountered disturbances. This refers to *out-of-distribution (OOD) generalization*, i.e., the ability to generalize to new datasets with different distributions from the training data [41]. We test the OOD generalization performance of parameter estimates using additional fault scenarios with randomized bus locations and fault clearing times. These

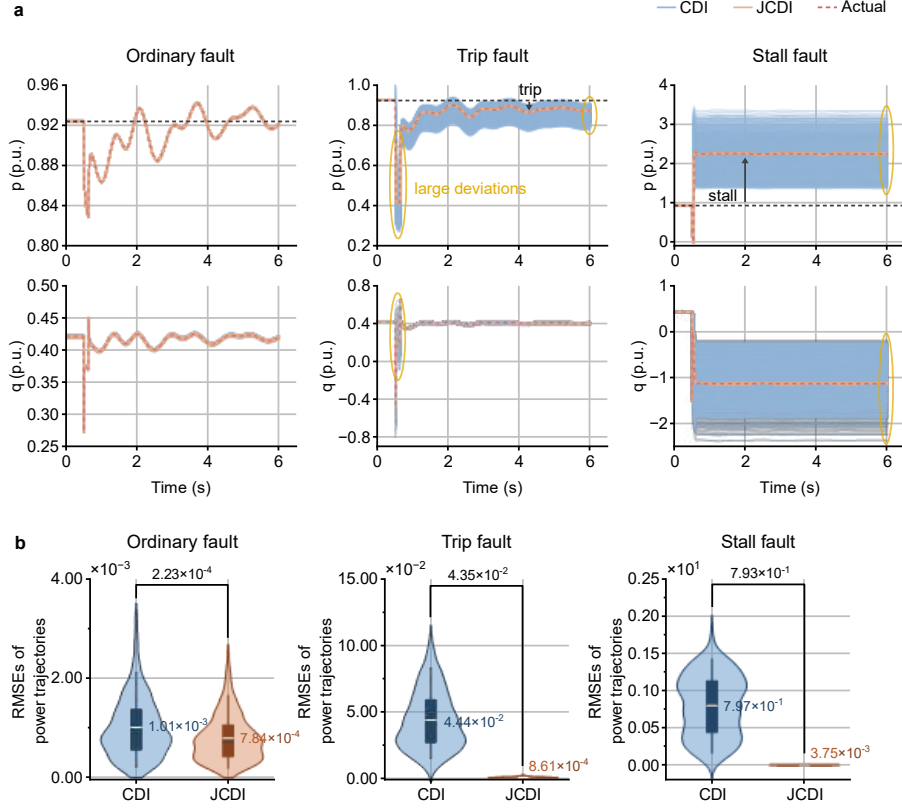


Fig. 5 Prediction results of dynamic responses. (a) Predicted power trajectories, including active power (p) and reactive power (q), under different fault events. They are obtained via grid simulations with estimated model parameters. (b) RMSEs of predicted power trajectories. The violin plots show the probability distributions of RMSEs with the widths representing the approximate frequency of data points in each region. The boxes inside span the intervals from the 25th to 75th percentile, while the white and black lines correspondingly represent the mean and median values.

scenarios comprise three groups: 100 ordinary fault events, 50 fault events inducing power electronic load tripping, and 10 events with motor D stalling. The test result is presented in Fig. 6. For CDI, the mean RMSEs of power trajectories for most testing cases within the ordinary fault group are close to the training case, while increased errors appear in several events, such as event 37. However, its performance deteriorates, exhibiting dispersed errors for tripping fault events and substantial increases in RMSE for stalling fault events. In contrast, JCDI maintains consistent and accurate predictions across all three testing groups. These results further demonstrate that JCDI produces parameter estimates with favorable generalization capability.

Comparison with other methods. To assess its superiority, we compare our developed JCDI with two mainstream methods for CLM parameterization: 1) RL implemented by deep Q-learning (DQN), and 2) SL using a combined neural network

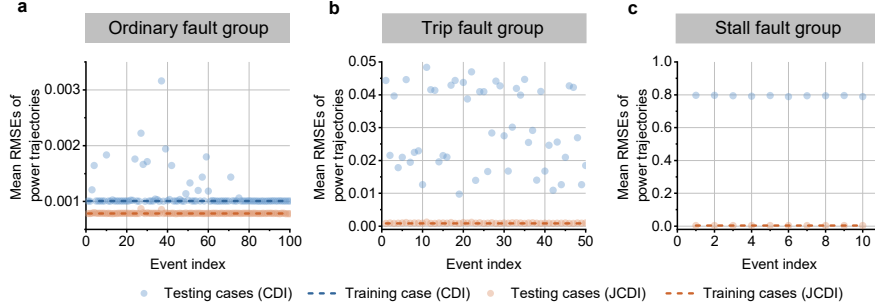


Fig. 6 Generalization results for additional testing fault events. Mean RMSEs of power trajectories are calculated using 1000 parameter estimate samples for each testing fault event. Blue and orange dots represent the mean RMSEs produced by CDI and JCDI respectively across different testing events. Dashed lines indicate the mean RMSEs for training events: **(a)** the ordinary fault event group, **(b)** the load tripping fault event group, and **(c)** the motor stalling fault event group.

architecture, including a Residual Network (ResNet) in series with a transformer encoder, designated as *Res-TFR*. This architecture matches JCDI’s neural network structure but infers model parameters directly, allowing the comparison to serve as an ablation study that demonstrates the advantage of the diffusion process. The details of the comparative algorithms are described in Supplementary Section 5 .

When inferring model parameters from specific power trajectories, Res-TFR produces a deterministic result, while DQN and diffusion models yield probabilistic solutions. In keeping with previous studies, we generate 1000 parameter estimates with diffusion models. Due to high computational burden for DQN, 100 solutions are deduced by rerunning the well-trained DQN agent. Table 1 summarizes the performance metrics of these approaches, including the mean estimation errors and the errors corresponding to the solutions that yield the minimum trajectory RMSEs under the ordinary fault event (min-traj cases). DQN tends to converge to local optima. It achieves the minimum trajectory RMSE at 5.30×10^{-3} for the ordinary fault event with the MARPE of model parameters exceeding 20%. Furthermore, these estimated parameters fail to effectively predict the dynamic trajectories for the trip and stall fault events. Res-TFR achieves a much lower parameter MARPE of 10.6%, which aligns with its loss function. However, the trajectory RMSE measures 3.55×10^{-3} for the ordinary fault and deteriorates further to 2.21×10^{-2} and 6.43×10^{-1} for trip and stall faults, respectively. Through the diffusion process, CDI probabilistically generates a solution set that encompasses various combinations of model parameters. This leads to the increase of parameter MARPE compared with Res-TFR. However, the trajectory RMSE under CDI reduces to 1.01×10^{-3} for the ordinary fault, indicating that CDI yields considerably comprehensive parameter estimates that reproduce the dynamic behavior of the system with greater precision. With the assistance of joint conditioning, JCDI achieves a mean parameter MARPE of 7.46%, representing a 58.6% reduction compared to CDI, while delivering the highest trajectory estimation accuracy across various fault events.

Table 1 Performance comparison of different parameterization methods

Parameterization methods	MARPEs of parameters	RMSEs of power trajectories		
		Ordinary fault	Trip fault	Stall fault
DQN (mean)	23.4%	6.46×10^{-3}	2.44×10^{-2}	1.21×10^{-1}
DQN (min-traj)	23.5%	5.30×10^{-3}	2.38×10^{-2}	1.55×10^{-1}
Res-TFR	10.6%	3.55×10^{-3}	2.21×10^{-2}	6.43×10^{-1}
CDI (mean)	18.0%	1.01×10^{-3}	4.44×10^{-2}	7.97×10^{-1}
CDI (min-traj)	19.8%	3.24×10^{-5}	7.81×10^{-2}	1.06
JCDI (mean)	7.46%	7.84×10^{-4}	8.61×10^{-4}	3.75×10^{-3}
JCDI (min-traj)	8.99%	4.18×10^{-5}	3.44×10^{-4}	5.47×10^{-3}

It is also worth noting that DQN requires performing transient simulation of the power system model repeatedly at each step within the episodes, which is time-consuming. In addition, this training process merely allows the agent to learn the parameter estimates that approximate one specific observation. However, for JCDI, we conduct parallel simulation to generate the dataset to train the diffusion model. After this is done, there is no need for additional physical simulation in both the training and inference processes. Therefore, JCDI solves the parameterization problem more efficiently. Furthermore, it learns the mapping between different observations and model parameters, providing a universal inverse solution of the system dynamics.

3 Discussion

This work presents JCDI, a novel probabilistic parameter estimation framework that mitigates the critical challenges posed by parameter non-uniqueness and cross-event generalization. Successful verification of JCDI has been achieved for CLM in power systems. Our comprehensive evaluation yields several key findings, including:

- The global sensitivity analysis reveals how the model parameters influence the system’s dynamic behavior differently under various grid faults. This insight inspires our approach to identify model parameters using multiple fault-induced disturbances.
- When conditioned on a single disturbance, the diffusion model generates a probabilistic solution encompassing multiple parameter sets that accurately reproduce power trajectories for the specific disturbance yet fail to generalize across diverse fault-induced disturbances, demonstrating the inherent non-identifiability of CLM parameters.
- JCDI produces more concentrated posterior distributions for model parameters, effectively addressing non-identifiable cases and significantly improving parameter estimation accuracy. Moreover, the model parameters estimated by JCDI accurately reproduce power trajectories under a group of testing fault events, verifying the favorable OOD generalization performance.
- Comparative studies demonstrate the superiority of diffusion models in solving the parameterization inverse problem compared to existing approaches. Diffusion models independently generate probabilistic solutions that accurately predict power trajectories and enable more precise and generalizable parameter estimation through

the joint conditioning mechanism. In addition, they eliminate the need for iterative forward simulations, providing more computationally efficient solutions.

Limitations and future work

Building on the effective demonstration of JCDDI for load modeling, potential extensions may involve parameterization for other electrical systems—such as power electronic converters and energy storage systems—as well as broader applications beyond electrical engineering and real-world deployment. However, several limitations warrant further discussion and represent important directions for future research.

Scalability Considerations. While our study examines JCDDI on CLM with 30 sensitive parameters, it is important to evaluate its scalability to higher-dimensional parameter spaces or more complex systems such as multi-area power grids. Empirical evidence from diffusion models (which operate successfully on 100K+ parameter spaces in image generation [27]) and transformer architectures (which routinely handle thousands of input tokens [42]) suggests that the JCDDI framework should scale effectively to systems with hundreds to low thousands of parameters, while ensuring computational tractability and training stability. Furthermore, it would be beneficial to reduce the computational requirements for large-scale implementations by exploring mitigation strategies such as subsystem division and using task-specific compact latent spaces [43, 44].

Time-critical Applications. Currently, the average inference time for JCDDI on a RTX 3090 GPU is measured at 1107 ms per batch (128 samples). Nevertheless, several well-established acceleration strategies can be readily applicable to our architecture. These include diffusion model subsampling techniques (e.g., DDIM [45]), lower precision arithmetic [46], model distillation methods [47], and architectural optimizations such as caching trajectory encoder outputs during iterative denoising. Together, these optimizations could yield at least an order of magnitude improvement in inference speed, making the framework practical for time-critical applications.

Discontinuous nonlinearity. Despite its high nonlinearity, CLM in our study represents an average model. When extending JCDDI to other systems, such as power electronic systems, their massive switching behavior induces significant discontinuous nonlinearities, which must be thoroughly considered when modeling electro-magnetic transient processes [48]. In this context, incorporating the discrete event information as physical priors into the framework would be a promising approach to improve its robustness in non-smooth dynamics [49–51].

Real-world deployment. Currently, JCDDI is developed and validated with synthetic data generated from CLM simulation. When deployed in the real world, several new concerns arise, necessitating further strategies to address them.

1) Phasor Measurement Unit (PMU) measurements in real power grids contain noise, which may have a negative impact on the estimation accuracy. It’s necessary to develop advanced filters that eliminate the maximum amount of noise. Additionally, JCDDI could be trained with noisy data that matches the real-world statistical characteristics.

2) CLM is an aggregated model that neglects the spatial distribution of individual loads and employs partially simplified dynamics. There will be discrepancies between simulation and real measurements, which may create a domain shift challenge [52].

Domain shift mitigation strategies [53, 54] would need to be applied to the JCIDI framework.

Comprehensive validation on real PMU data represents an important direction for future work to establish practical deployment readiness.

4 Methods

Problem formulation. The measurement-based parameterization for CLM represents a classical inverse problem, where model parameters are derived from observed dynamic responses, as formulated in equation (4).

$$y = F(\theta) \Rightarrow \theta = F^{-1}(y), \quad (4)$$

where F is the forward operator, F^{-1} is inverse operator, θ denotes the model parameters, and y represents the observation. The observation comprises active and reactive powers measured at the interconnection point between the transmission system and power loads (Fig. 1). The observation vector y can be expressed as equation (5).

$$\begin{aligned} y &= [p, q] \\ p &= [p_1, p_2, \dots, p_T] \\ q &= [q_1, q_2, \dots, q_T], \end{aligned} \quad (5)$$

where p and q represent the active and reactive power trajectories, respectively.

Bayesian inference provides a probabilistic approach for solving this inverse problem. Based on Bayes' theorem [55], the posterior distribution of model parameters, conditioned on the specific observation, is proportional to the product of the likelihood function and the prior parameter distribution, which is formalized in equation (6).

$$P(\theta|y_0) = \frac{P(y_0|\theta) \cdot P(\theta)}{P(y_0)} \propto P(y_0|\theta) \cdot P(\theta), \quad (6)$$

where y_0 denotes the conditioned observation, $P(\theta)$ and $P(\theta|y_0)$ respectively represent the prior and posterior distributions of model parameters. The likelihood function $P(y_0|\theta)$ quantifies the probability of observing y_0 , given specific parameter values θ . $P(y_0)$ represents the probability of observing y_0 across all the model parameters, serving as a constant.

Model development. The denoising diffusion probabilistic model (DDPM) is an advanced latent variable model trained using variational inference [27]. The posterior is approximated with a parametric family of distributions, eliminating the need to compute the likelihood function [56]. Inspired by non-equilibrium thermodynamics, DDPM transforms the original data $x_0 \sim q(x_0)$ into a latent representation $x_T \sim N(\mu, \sigma^2)$ by gradually adding random noise then learns a Markov chain $p_\omega(x_{0:T})$ to reverse this process. The reverse process is implemented via a denoising neural network that estimates and progressively removes the added noise, enabling the reconstruction of the original data distribution through the transition from x_T back to x_0 .

As an extension, the conditional DDPM enables controlled data generation that satisfies specific constraints. The conditioning is achieved by modifying the reverse process to depend on both the noisy input and the condition. Specifically, the denoising neural network $\varepsilon_\omega(x_t, t)$ is augmented to accept an additional condition input y , becoming $\varepsilon_\omega(x_t, t, y)$. Our JCDI applies the diffusion and reverse processes to the model parameter space and uses the measured power trajectories as conditions to guide the generation process. Therefore, the joint probability of reverse process becomes $p_\omega(x_{0:T}|y)$, allowing it to learn a mapping from observed system behaviors to the underlying model parameters that generate them.

Network architecture. We introduce the Inverse Grid Transformer (IGT), a novel denoising neural network architecture based on the transformer encoder (illustrated in Fig. 2). Originally developed for natural language processing, the Transformer, has revolutionized the field while achieving remarkable success across multiple domains. It converts the input, such as text, into numerical representations (tokens) and captures long-range dependencies among different tokens based on the attention mechanism [57].

In our architecture, the transformer encoder receives three types of inputs: 1) model parameters that are being denoised, 2) encoded power trajectories, and 3) encoded diffusion time step t . We do not add positional encoding here as the inputs have no natural distance measure between them. Each input is tokenized with a separate linear encoder module (tokenizer). The power trajectories act as the conditions. Before being converted into transformer tokens, they are processed through the trajectory encoders. The trajectory encoders employ ResNet architectures and extract latent features from the raw two-dimensional power trajectories [58]. The diffusion step t is sinusoidally embedded and incorporated as a part of inputs to provide information about noise level.

The transformer encoder is composed of a stack of layers, each containing a multi-head attention layer followed by a feed forward network. Layer normalization is utilized within each sublayer. The attention model calculates the correlation (attention weight) of input elements then produces the output representation through weighted summation of the inputs. Specifically, each input token is transformed into three variables, query Q , key K , and value V , by linear projections in equation (7). The model computes the attention scores by taking the dot product of the queries Q and keys K , which measures the similarity between them. The attention weights are then obtained by applying a softmax operation to the attention scores, ensuring that the attention weights sum up to 1 for each query. The model’s output is an attention-weighted sum of values V as expressed by equation (8). On this basis, the multi-head attention is implemented by performing several attention functions with different linear projections in parallel then concatenating the outputs. Based on the multi-head attention mechanism, the denoising neural network seeks to represent the correlations among the CLM parameters, as well as the relationships between model parameters and conditioned power trajectories, enhancing parameter estimation performance.

$$Q = W_Q \cdot X, K = W_K \cdot X, V = W_V \cdot X, \quad (7)$$

$$\text{Attention}(Q, K, V) = \text{softmax}\left(\frac{QK^T}{\sqrt{d_k}}\right) \cdot V, \quad (8)$$

where W_Q , W_K , and W_V are the transformation matrices; X represents the input tokens; and d_k denotes the dimension of keys.

Multi-event joint conditioning. Due to parameter non-uniqueness, the traditional parameter estimation methods using a single disturbance may deduce various combinations of parameters, while some are not generalizable to other disturbances. Here, we address this challenge by the multi-event joint conditioning mechanism, where power trajectories under different fault-induced disturbances simultaneously serve as the condition inputs to deduce model parameters. Therefore, the posterior distribution of model parameters will be the joint probability that satisfies multiple trajectory conditions, which equals the product of individual ones due to the independence of fault events as expressed by equation (9). This serves to reduce parameter estimation uncertainties, thereby producing more robust and generalizable solutions.

$$\begin{aligned} P(\theta|y_{1,0}, y_{2,0}, \dots, y_{N,0}) &= \frac{P(y_{1,0}, y_{2,0}, \dots, y_{N,0}|\theta) \cdot P(\theta)}{P(y_{1,0}, y_{2,0}, \dots, y_{N,0})} \\ &= \frac{P(y_{1,0}|\theta) \cdot P(y_{2,0}|\theta) \cdot \dots \cdot P(y_{N,0}|\theta) \cdot P(\theta)}{P(y_{1,0}) \cdot P(y_{2,0}) \cdot \dots \cdot P(y_{N,0})} \\ &\propto P(y_{1,0}|\theta) \cdot P(y_{2,0}|\theta) \cdot \dots \cdot P(y_{N,0}|\theta) \cdot P(\theta), \end{aligned} \quad (9)$$

where $y_{i,0}$, $i = 1:N$ denotes the measurement under the i -th fault event.

Training and inference procedures. In the training stage, we randomly sample diffusion step $t \sim \text{Uniform}(\{1, \dots, T\})$, and Gaussian noise $\varepsilon \sim \mathcal{N}(0, I)$ then transform the original model parameters x_0 into the noised latent x_t expressed by equation (10).

$$x_t = \sqrt{\bar{\alpha}_t}x_0 + \sqrt{1 - \bar{\alpha}_t}\varepsilon, \quad (10)$$

where $\alpha_t = 1 - \beta_t$, $\bar{\alpha}_t = \prod_{s=1}^t \alpha_s$. β_t represents the variance schedule of the noising process.

The noise latent x_t , diffusion step t , and conditioned power trajectories y are simultaneously input into the neural network IGT, which predicts the Gaussian noise as $\varepsilon_\omega(x_t, t, y)$. Then, the denoising neural network is trained by minimizing the MSE between the predicted and actually added Gaussian noises, which is calculated by equation (11).

$$\min \mathbb{E}_{x_0, \varepsilon} \|\varepsilon - \varepsilon_\omega(x_t, t, y)\|^2. \quad (11)$$

After completing the training process, we use the well-trained model to infer model parameters given the desired observations. In this inference stage, we start with randomly sampling $x_T \sim \mathcal{N}(0, I)$. At each step $t = T, \dots, 1$, we use the desired power trajectories y_0 as the condition to calculate the added noise with the trained neural network. Then, we subtract it from the latent variable x_t , and compute x_{t-1} with equation (12). Therefore, the latent variables can be gradually denoised, and the noiseless estimation of model parameters x_0 are obtained at the final step. Due to the probabilistic nature of the diffusion and reverse process, we will deduce different parameter estimation solutions when repeatedly running the diffusion model, thereby acquiring the posterior distribution of the predicted model parameters.

$$x_{t-1} = \frac{1}{\sqrt{\alpha_t}} \left(x_t - \frac{1 - \alpha_t}{\sqrt{1 - \bar{\alpha}_t}} \varepsilon_\omega(x_t, t, y_0) \right) + \sigma_t z, \quad (12)$$

where $\sigma_t = \sqrt{\beta_t}$, $z \sim \mathcal{N}(0, I)$.

Data availability

The data used in this work will be made available prior to publication.

Code availability

The code developed for this work will be made available prior to publication.

References

- [1] Tarantola, A.: Inverse Problem Theory and Methods for Model Parameter Estimation. SIAM: Society for Industrial and Applied Mathematics, Philadelphia (2005)
- [2] Lederman, D., Patel, R., Itani, O., Rotstein, H.G.: Parameter estimation in the age of degeneracy and unidentifiability. *Mathematics* **10**(2), 170 (2022)
- [3] World energy outlook 2024. Technical report, International Energy Agency (2024)
- [4] Heerden, R., Edelenbosch, O.Y., Daioglou, V., Le Gallic, T., Baptista, L.B., Di Bella, A., Colelli, F.P., Emmerling, J., Fragkos, P., Hasse, R., et al.: Demand-side strategies enable rapid and deep cuts in buildings and transport emissions to 2050. *Nature Energy*, 1–15 (2025)
- [5] Powell, S., Cezar, G.V., Min, L., Azevedo, I.M., Rajagopal, R.: Charging infrastructure access and operation to reduce the grid impacts of deep electric vehicle adoption. *Nature Energy* **7**(10), 932–945 (2022)
- [6] Jacob, R.A., Paul, S., Chowdhury, S., Gel, Y.R., Zhang, J.: Real-time outage management in active distribution networks using reinforcement learning over graphs. *Nature Communications* **15**(1), 4766 (2024)
- [7] Kim, J.-K., Kang, J., Shim, J.W., Kim, H., Shin, J., Kang, C., Hur, K.: Dynamic performance modeling and analysis of power grids with high levels of stochastic and power electronic interfaced resources. *Proceedings of the IEEE* **111**(7), 854–872 (2023) <https://doi.org/10.1109/JPROC.2023.3284890>
- [8] Arif, A., Wang, Z., Wang, J., Mather, B., Bashualdo, H., Zhao, D.: Load modeling—a review. *IEEE Transactions on Smart Grid* **9**(6), 5986–5999 (2018) <https://doi.org/10.1109/TSG.2017.2700436>

- [9] Aster, R.C., Borchers, B., Thurber, C.H.: Chapter three - rank deficiency and ill-conditioning. In: Aster, R.C., Borchers, B., Thurber, C.H. (eds.) *Parameter Estimation and Inverse Problems (Third Edition)*, Third edition edn., pp. 55–91. Elsevier, Amsterdam (2019)
- [10] Piani, S., Farrell, P., Lei, W., Rotundo, N., Heltai, L.: Data-driven solutions of ill-posed inverse problems arising from doping reconstruction in semiconductors. *Applied Mathematics in Science and Engineering* **32**(1), 2323626 (2024)
- [11] Engl, H.W., Groetsch, C.W.: *Inverse and Ill-posed Problems*. Elsevier, Amsterdam (2014)
- [12] Wang, H., Fu, T., Du, Y., Gao, W., Huang, K., Liu, Z., Chandak, P., Liu, S., Van Katwyk, P., Deac, A., *et al.*: Scientific discovery in the age of artificial intelligence. *Nature* **620**(7972), 47–60 (2023)
- [13] Hamann, H.F., Gjorgiev, B., Brunschwiler, T., Martins, L.S., Puech, A., Varbella, A., Weiss, J., Bernabe-Moreno, J., Massé, A.B., Choi, S.L., *et al.*: Foundation models for the electric power grid. *Joule* **8**(12), 3245–3258 (2024)
- [14] Aarts, G., Fukushima, K., Hatsuda, T., Ipp, A., Shi, S., Wang, L., Zhou, K.: Physics-driven learning for inverse problems in quantum chromodynamics. *Nature Reviews Physics*, 1–10 (2025)
- [15] Raissi, M., Perdikaris, P., Karniadakis, G.E.: Physics-informed neural networks: A deep learning framework for solving forward and inverse problems involving nonlinear partial differential equations. *Journal of Computational physics* **378**, 686–707 (2019)
- [16] Kadeethum, T., O’Malley, D., Fuhg, J.N., Choi, Y., Lee, J., Viswanathan, H.S., Bouklas, N.: A framework for data-driven solution and parameter estimation of pdes using conditional generative adversarial networks. *Nature Computational Science* **1**(12), 819–829 (2021)
- [17] Gabbard, H., Messenger, C., Heng, I.S., Tonolini, F., Murray-Smith, R.: Bayesian parameter estimation using conditional variational autoencoders for gravitational-wave astronomy. *Nature Physics* **18**(1), 112–117 (2022)
- [18] Wang, X., Wang, Y., Shi, D., Wang, J., Wang, Z.: Two-stage WECC composite load modeling: A double deep q-learning networks approach. *IEEE Transactions on Smart Grid* **11**(5), 4331–4344 (2020) <https://doi.org/10.1109/TSG.2020.2988171>
- [19] Bu, F., Ma, Z., Yuan, Y., Wang, Z.: WECC composite load model parameter identification using evolutionary deep reinforcement learning. *IEEE Transactions on Smart Grid* **11**(6), 5407–5417 (2020) <https://doi.org/10.1109/TSG.2020.3008730>
- [20] Xie, J., Ma, Z., Dehghanpour, K., Wang, Z., Wang, Y., Diao, R., Shi, D.:

- Imitation and transfer q-learning-based parameter identification for composite load modeling. *IEEE Transactions on Smart Grid* **12**(2), 1674–1684 (2021) <https://doi.org/10.1109/TSG.2020.3025509>
- [21] Afrasiabi, S., Afrasiabi, M., Jarrahi, M.A., Mohammadi, M., Aghaei, J., Javadi, M.S., Shafie-Khah, M., Catalão, J.P.S.: Wide-area composite load parameter identification based on multi-residual deep neural network. *IEEE Transactions on Neural Networks and Learning Systems* **34**(9), 6121–6131 (2023) <https://doi.org/10.1109/TNNLS.2021.3133350>
- [22] Hu, J., Wang, Q., Ye, Y., Tang, Y.: Toward online power system model identification: A deep reinforcement learning approach. *IEEE Transactions on Power Systems* **38**(3), 2580–2593 (2023) <https://doi.org/10.1109/TPWRS.2022.3180415>
- [23] Khodayar, M., Wang, J.: Probabilistic time-varying parameter identification for load modeling: A deep generative approach. *IEEE Transactions on Industrial Informatics* **17**(3), 1625–1636 (2021) <https://doi.org/10.1109/TII.2020.2971014>
- [24] Tan, B., Zhao, J., Duan, N.: Amortized bayesian parameter estimation approach for wecc composite load model. *IEEE Transactions on Power Systems* **39**(1), 1517–1529 (2024) <https://doi.org/10.1109/TPWRS.2023.3250579>
- [25] Hu, J., Wang, Q., Ye, Y., Tang, Y.: Toward online power system model identification: A deep reinforcement learning approach. *IEEE Transactions on Power Systems* **38**(3), 2580–2593 (2023) <https://doi.org/10.1109/TPWRS.2022.3180415>
- [26] Xie, J., Ma, Z., Dehghanpour, K., Wang, Z., Wang, Y., Diao, R., Shi, D.: Imitation and transfer q-learning-based parameter identification for composite load modeling. *IEEE Transactions on Smart Grid* **12**(2), 1674–1684 (2021) <https://doi.org/10.1109/TSG.2020.3025509>
- [27] Ho, J., Jain, A., Abbeel, P.: Denoising diffusion probabilistic models. *Advances in neural information processing systems* **33**, 6840–6851 (2020)
- [28] Yang, L., Zhang, Z., Song, Y., Hong, S., Xu, R., Zhao, Y., Zhang, W., Cui, B., Yang, M.-H.: Diffusion models: A comprehensive survey of methods and applications. *ACM Computing Surveys* **56**(4), 1–39 (2023)
- [29] Dhariwal, P., Nichol, A.: Diffusion models beat gans on image synthesis. *Advances in neural information processing systems* **34**, 8780–8794 (2021)
- [30] Du, H., Zhang, R., Liu, Y., Wang, J., Lin, Y., Li, Z., Niyato, D., Kang, J., Xiong, Z., Cui, S., Ai, B., Zhou, H., Kim, D.I.: Enhancing deep reinforcement learning: A tutorial on generative diffusion models in network optimization. *IEEE Communications Surveys & Tutorials* **26**(4), 2611–2646 (2024) <https://doi.org/10.1109/COMST.2024.3400011>

- [31] Price, I., Sanchez-Gonzalez, A., Alet, F., Andersson, T.R., El-Kadi, A., Masters, D., Ewalds, T., Stott, J., Mohamed, S., Battaglia, P., *et al.*: Probabilistic weather forecasting with machine learning. *Nature* **637**(8044), 84–90 (2025)
- [32] Daras, G., Chung, H., Lai, C.-H., Mitsufuji, Y., Ye, J.C., Milanfar, P., Dimakis, A.G., Delbracio, M.: A Survey on Diffusion Models for Inverse Problems. Preprint at <https://arxiv.org/abs/2410.00083> (2024)
- [33] Kawar, B., Elad, M., Ermon, S., Song, J.: Denoising diffusion restoration models. *Advances in Neural Information Processing Systems* **35**, 23593–23606 (2022)
- [34] WECC composite load model with DG specification. Technical report, Western Electricity Coordinating Council (WECC) (2015)
- [35] Porthiyas, J., Nussey, D., Beauchemin, C.A.A., Warren, D.C., Quirouette, C., Wilkie, K.P.: Practical parameter identifiability and handling of censored data with bayesian inference in mathematical tumour models. *npj Systems Biology and Applications* **10**(89) (2024)
- [36] Shuangcheng, W.: *Bayesian Network Learning, Inference and Applications*. Lixin Accounting Press, Shanghai (2010)
- [37] Paninski, L.: Estimation of entropy and mutual information. *Neural Computation* **15**(6), 1191–1253 (2003) <https://doi.org/10.1162/089976603321780272>
- [38] Kraskov, A., Stögbauer, H., Grassberger, P.: Estimating mutual information. *Phys. Rev. E* **69**, 066138 (2004) <https://doi.org/10.1103/PhysRevE.69.066138>
- [39] scikit-learn developers: mutual_info_regression. https://scikit-learn.org/stable/modules/generated/sklearn.feature_selection.mutual_info_regression.html (2025)
- [40] Myttenaere, A., Golden, B., Le Grand, B., Rossi, F.: Mean absolute percentage error for regression models. *Neurocomputing* **192**, 38–48 (2016) <https://doi.org/10.1016/j.neucom.2015.12.114>
- [41] Liu, J., Shen, Z., He, Y., Zhang, X., Xu, R., Yu, H., Cui, P.: Towards Out-Of-Distribution Generalization: A Survey. Preprint at <https://arxiv.org/abs/2108.13624> (2023)
- [42] Touvron, H., Lavril, T., Izacard, G., Martinet, X., Lachaux, M., Lacroix, T., Rozière, B., Goyal, N., Hambro, E., Azhar, F., Rodriguez, A., Joulin, A., Grave, E., Lample, G.: Llama: Open and efficient foundation language models. *CoRR* **abs/2302.13971** (2023) <https://doi.org/10.48550/ARXIV.2302.13971>
- [43] Hinton, G.E., Salakhutdinov, R.R.: Reducing the dimensionality of data with

neural networks. *science* **313**(5786), 504–507 (2006)

- [44] Alemi, A.A., Fischer, I., Dillon, J.V., Murphy, K.: Deep variational information bottleneck. In: *International Conference on Learning Representations* (2017). <https://openreview.net/forum?id=HyxQzBceg>
- [45] Song, J., Meng, C., Ermon, S.: Denoising diffusion implicit models. In: *International Conference on Learning Representations* (2021). <https://openreview.net/forum?id=St1giarCHLP>
- [46] Micikevicius, P., Narang, S., Alben, J., Diamos, G., Elsen, E., Garcia, D., Ginsburg, B., Houston, M., Kuchaiev, O., Venkatesh, G., Wu, H.: Mixed precision training. In: *International Conference on Learning Representations* (2018). <https://openreview.net/forum?id=r1gs9JgRZ>
- [47] Salimans, T., Ho, J.: Progressive distillation for fast sampling of diffusion models. In: *International Conference on Learning Representations* (2022). <https://openreview.net/forum?id=TldIXlpzhol>
- [48] Zhengming Zhao, L.Y. Bochen Shi: *Dynamic Characterization and Control of Power Electronic Hybrid Systems*. China Machine Press, Beijing (2024)
- [49] Hao, Z., Liu, S., Zhang, Y., Ying, C., Feng, Y., Su, H., Zhu, J.: *Physics-Informed Machine Learning: A Survey on Problems, Methods and Applications* (2023). <https://arxiv.org/abs/2211.08064>
- [50] Karniadakis, G.E., Kevrekidis, I.G., Lu, L., Perdikaris, P., Wang, S., Yang, L.: Physics-informed machine learning. *Nature Reviews Physics* **3**(6), 422–440 (2021)
- [51] Zheng, J., Wang, H., Zeng, Y., Mou, D., Zhang, X., Li, H., Vazquez, S., Franquelo, L.G.: Physics-Embedded Neural ODEs for Sim2Real Edge Digital Twins of Hybrid Power Electronics Systems (2025). <https://arxiv.org/abs/2508.02887>
- [52] Quiñonero-Candela, J., Sugiyama, M., Schwaighofer, A., Lawrence, N.D.: *Dataset Shift in Machine Learning*. Mit Press, Cambridge (2022)
- [53] Csurka, G.: In: Csurka, G. (ed.) *A Comprehensive Survey on Domain Adaptation for Visual Applications*, pp. 1–35. Springer, Cham (2017). https://doi.org/10.1007/978-3-319-58347-1_1 . https://doi.org/10.1007/978-3-319-58347-1_1
- [54] Zhuang, F., Qi, Z., Duan, K., Xi, D., Zhu, Y., Zhu, H., Xiong, H., He, Q.: A comprehensive survey on transfer learning. *Proc. IEEE* **109**(1), 43–76 (2021) <https://doi.org/10.1109/JPROC.2020.3004555>
- [55] Murphy, K.P.: *Machine Learning: a Probabilistic Perspective*. MIT press, Cambridge, MA (2012)

- [56] Nemani, V., Biggio, L., Huan, X., Hu, Z., Fink, O., Tran, A., Wang, Y., Zhang, X., Hu, C.: Uncertainty quantification in machine learning for engineering design and health prognostics: A tutorial. *Mechanical Systems and Signal Processing* **205**, 110796 (2023)
- [57] Vaswani, A., Shazeer, N., Parmar, N., Uszkoreit, J., Jones, L., Gomez, A.N., Kaiser, L.u., Polosukhin, I.: Attention is all you need. In: Guyon, I., Luxburg, U.V., Bengio, S., Wallach, H., Fergus, R., Vishwanathan, S., Garnett, R. (eds.) *Advances in Neural Information Processing Systems*, vol. 30. Curran Associates, Inc., New York (2017)
- [58] He, K., Zhang, X., Ren, S., Sun, J.: Deep residual learning for image recognition. In: *Proceedings of the IEEE Conference on Computer Vision and Pattern Recognition*, pp. 770–778 (2016)

Acknowledgments

This work was supported by the Advanced Grid Modeling Program, Office of Electricity of the U.S. Department of Energy under Agreement 39917.

Author contributions

Competing interests

Additional information

Supplementary information. This work contains supplementary material, which has been uploaded.

Supplementary Information for

**Diffusion Model-based Parameter
Estimation in Dynamic Power Systems**

Contents

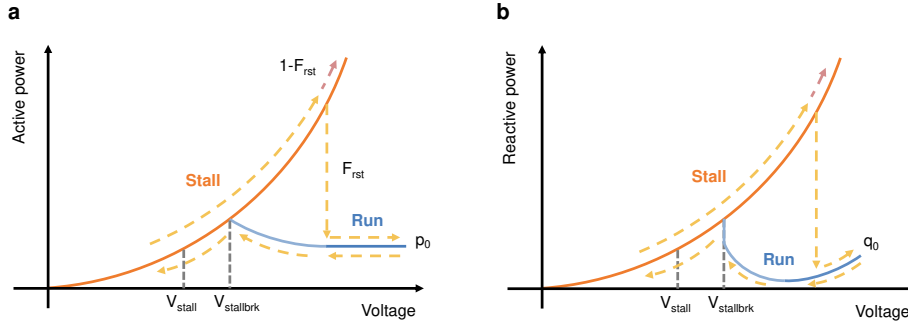
1	CMPLDWG compositions and characteristics	2
2	CMPLDWG dynamic simulation	4
3	Parameter sensitivity analysis	5
4	Supplementary information of JCDI	9
5	Supplementary information of comparative algorithms	10

1 CMPLDWG compositions and characteristics

To address the rapid evolution of electric power loads, Western Electricity Coordinating Council (WECC) has developed an advanced CLM – composite load model with distributed generation (CMPLDWG) [1]. It consists of three, three-phase induction motors with different characteristics (motors A, B, and C); one single-phase induction motor (motor D); one power electronic load; one static load; and one distributed energy resource (DER) [2]. This allows it to represent different electric characteristics of power loads and flexibly change the fractions of each composition according to the actual power loads.

Motor A characterizes the three-phase induction motors that drive low-inertia constant torque loads. Typical examples include positive displacement compressors and pumps [3]. Motor B represents the high-inertia variable torque loads, such as large fans, and motor C is used to model the low-inertia variable torque loads, such as centrifugal pumps. They are modeled by fifth-order differential-algebraic equations based on electromagnetic and electromechanical equations with different parameters [4]. Motor D represents the single-phase induction motor, such as residential air-conditioners and heat ventilation. In CLM, it is developed as a “performance model” based on laboratory tests. The static loads are characterized by the ZIP model, which consists of constant impedance (Z), constant current (I), and constant power (P) components. The power electronic load represents an aggregation of inverter-interfaced or electronic coupled loads, such as consumer electronic devices (e.g., computers). Supplementary Figure 2 depicts the power-voltage relationship of electronic load. DER version A (DER_A) is newly developed in load modeling to represent the aggregation of inverter-based generation (e.g., photovoltaic) [1]. Its block diagram and specification refers to [5].

Stalling behavior of a single-phase induction motor. Single-phase motors are prone to stalling when compared with three-phase motors due to their low torque characteristics at low voltage levels. There is insufficient motor torque to overcome the load torque. Therefore, the motor stops. Supplementary Figure 1 shows the power change of motor D during the stalling and recovering processes.



Supplementary Fig. 1 Motor D power changes when stalling. The blue line illustrates motor D operating in run state, while the orange line represents its power change in stall state. The yellow arrow indicates the state transition process: (a) active power and (b) reactive power.

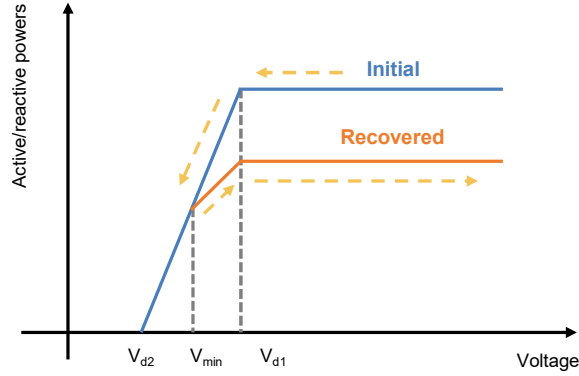
When the terminal voltage drops lower than the motor stalling voltage V_{stall} for a time duration of T_{stall} , motor D transitions from run state to stall state. The active and reactive powers of motor D are proportional to the square of voltage in stall state (as expressed by (Supplementary Equation 1)), leading to high power consumption.

$$\begin{aligned} p &= V^2/R_{stall} \\ q &= -V^2/X_{stall} \end{aligned} \quad (\text{Supplementary Equation 1})$$

where R_{stall} and X_{stall} respectively denote the stall resistance and reactance.

When the terminal voltage recovers and becomes higher than the restarting voltage V_{rst} of the stalled motors for a time duration of T_{rst} , a portion (F_{rst}) of the motor D loads transition to run state, while the rest remains in stall state.

Tripping behavior of power electronic load. As shown in Supplementary Fig. 2, when the terminal voltage maintains above V_{d1} , the electronic load consumes constant active and reactive power. However, when the voltage drops lower than V_{d1} , the powers reduce linearly, which indicates the undervoltage trip of the power electronic loads. The powers become zero when the voltage reduces to V_{d2} . As the voltage recovers, there will be a certain fraction of loads reconnecting to the system. Thus, the active and reactive powers increase and stabilize at values lower than their initial levels, which is calculated by (Supplementary Equation 2).



Supplementary Fig. 2 Power changes of power electronic load when tripping. The blue line illustrates its powers during initial operation and the occurrence of tripping, while the orange line represents power changes throughout the recovery process. The yellow arrow indicates the state transition process.

$$\begin{aligned} Fvl_{rec} &= \frac{(V_{min}-V_{d2})+frcel \cdot (V_{d1}-V_{min})}{V_{d1}-V_{d2}} \\ p_{el,rec} &= p_{el,0} \cdot Fvl_{rec} \\ q_{el,rec} &= q_{el,0} \cdot Fvl_{rec} \end{aligned} \quad (\text{Supplementary Equation 2})$$

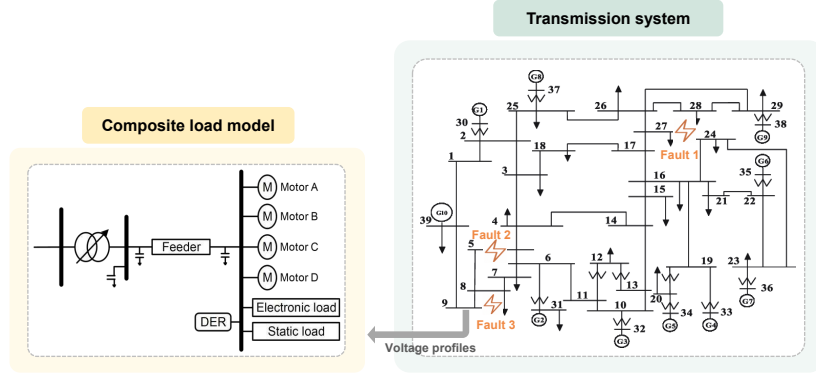
where V_{min} is the minimum value of the terminal voltage during the tripping process, $frcel$ is the fraction of electronic loads that reconnect to the system after voltage

recovery, and Fvl_{rec} denotes the proportion of recovered powers. $p_{el,0}$ and $q_{el,0}$ respectively represent the initial active and reactive powers. $p_{el,rec}$ and $q_{el,rec}$ designate the recovered powers.

2 CMPLDWG dynamic simulation

To implement dynamic simulation, CMPLDWG is supplied by the bulk transmission system, as depicted in Supplementary Fig. 3. The transmission system represents an IEEE 39-bus system established in ePHASORSIM. The voltage profiles at Bus 9, the point of interconnection (POI), of the transmission system are fed into CMPLDWG.

We simulate three-phase-to-ground electrical faults in the transmission system. Three separate fault events are implemented, each with a **fault impedance** of $1 \times 10^{-5} \Omega$ at different bus locations [6]. The corresponding fault clearing times and locations are detailed in Supplementary Table 1. The fault clearing times are selected from a relatively wide yet realistic range, ensuring our analysis encompasses a comprehensive set of potential grid conditions. Based on the empirical value of 3-6 cycles, the fault clearing time can also be influenced by the uncertain delays, the voltage level of the transmission systems, as well as the advancement of modern protection technologies [7, 8].



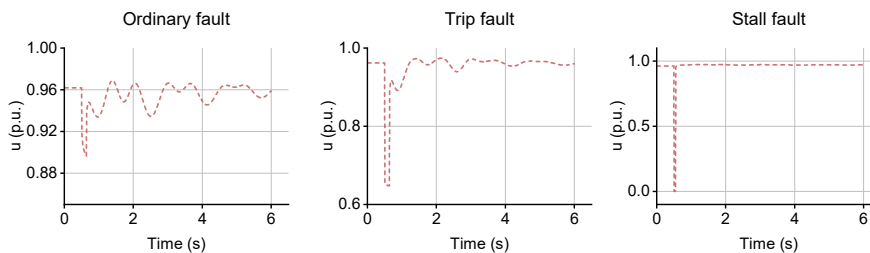
Supplementary Fig. 3 Schematic diagram of CMPLDWG dynamic simulation. Load model represented by CMPLDWG is supplied by the IEEE 39-bus transmission system. Electrical faults are simulated at different bus locations in the transmission system.

Supplementary Table. 1 List of electrical fault events

Fault index	Bus location	Clearing time	Dynamic characteristics
No. 1	27	135 ms	Ordinary
No. 2	5	135 ms	Power electronic load tripping
No. 3	9	44 ms	Motor D stalling

We use the voltage profiles under electric fault disturbances as the inputs, and compare the power responses of the CMPLDWG with different parameter estimates. This approach is well-established, as evidenced by its application in [4, 5] to evaluate the dynamic responses of load models and distributed energy resources (DERs).

The voltage profiles under the three electric fault events are depicted in Supplementary Fig. 4. The first electric fault (ordinary fault) occurs on Bus 27, which is far from the POI. Therefore, this fault disturbance induces a minor effect, the voltage reduces slightly during the fault (minimum to 0.90 p.u.). The second electric fault (trip fault) occurs on Bus 5, which is much closer to the POI and the load model. As a result, the voltage drops to 0.65 p.u., which is below the voltage tripping threshold ($V_{d1}=0.8$ p.u.) for the power electronic load in CMPLDWG, as illustrated in Supplementary Fig. 2 [3]. This causes the power electronic load to trip during the fault event. The third electric fault (stall fault) is located on the POI. The voltage becomes zero during the fault interval (44 ms). This induces the stalling behavior of motor D: the voltage drops lower than V_{stall} for a time duration of T_{stall} [3]. In our study, $V_{stall} = 0.6$ p.u., $T_{stall} = 30$ ms.



Supplementary Fig. 4 Voltage trajectories under different fault disturbances. Voltage profiles are measured at the POI. They exhibit distinct voltage drops and recovery processes when electrical faults occur at different bus locations.

3 Parameter sensitivity analysis

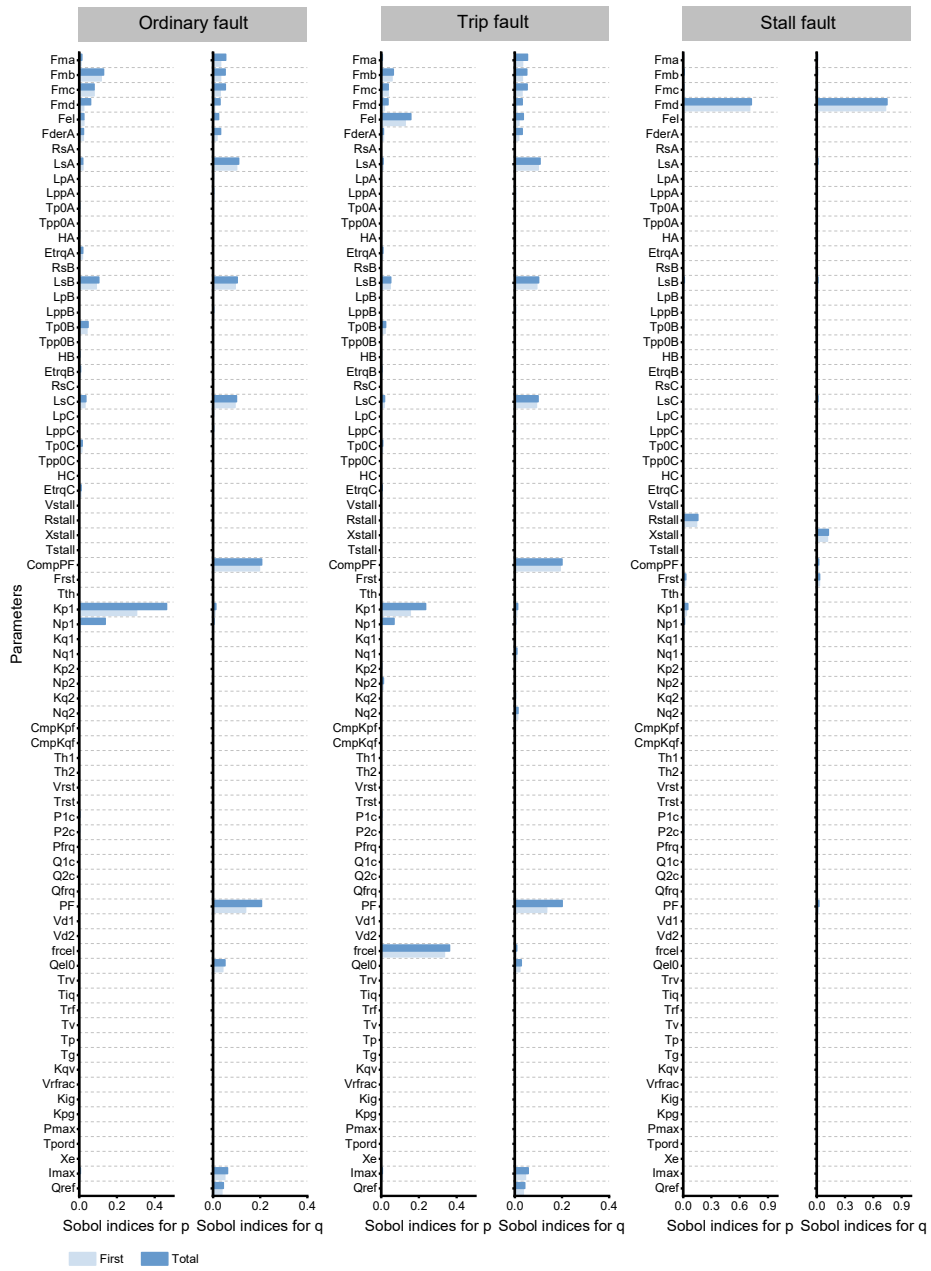
In this work, sensitivity analysis based on Sobol’s method [9–13] is performed for parameter reduction. Sobol’s method is a variance-based global sensitivity analysis method, which decomposes the variance of output into contributions from individual input parameters and their interactions. Therein, first-order index measures the individual effect of the input variable on the output. Second-order index indicates the effect of interaction between different input variables. The total-effect index calculates the full contribution of the input variable on the output variance, which is the sum of the indices of different orders.

To gain insight into the influences of model parameters on the system dynamic behavior under different fault-induced disturbances, we calculate the Sobol indices of CMPLDWG parameters for active and reactive power trajectories under the ordinary, trip, and stall faults (Supplementary Fig. 5). Then, the model parameters are ranked according to their total-effect indices (Supplementary Fig. 6). Most of the parameters present consistent sensitivity under different fault events. However, fr_{cel} and F_{el}

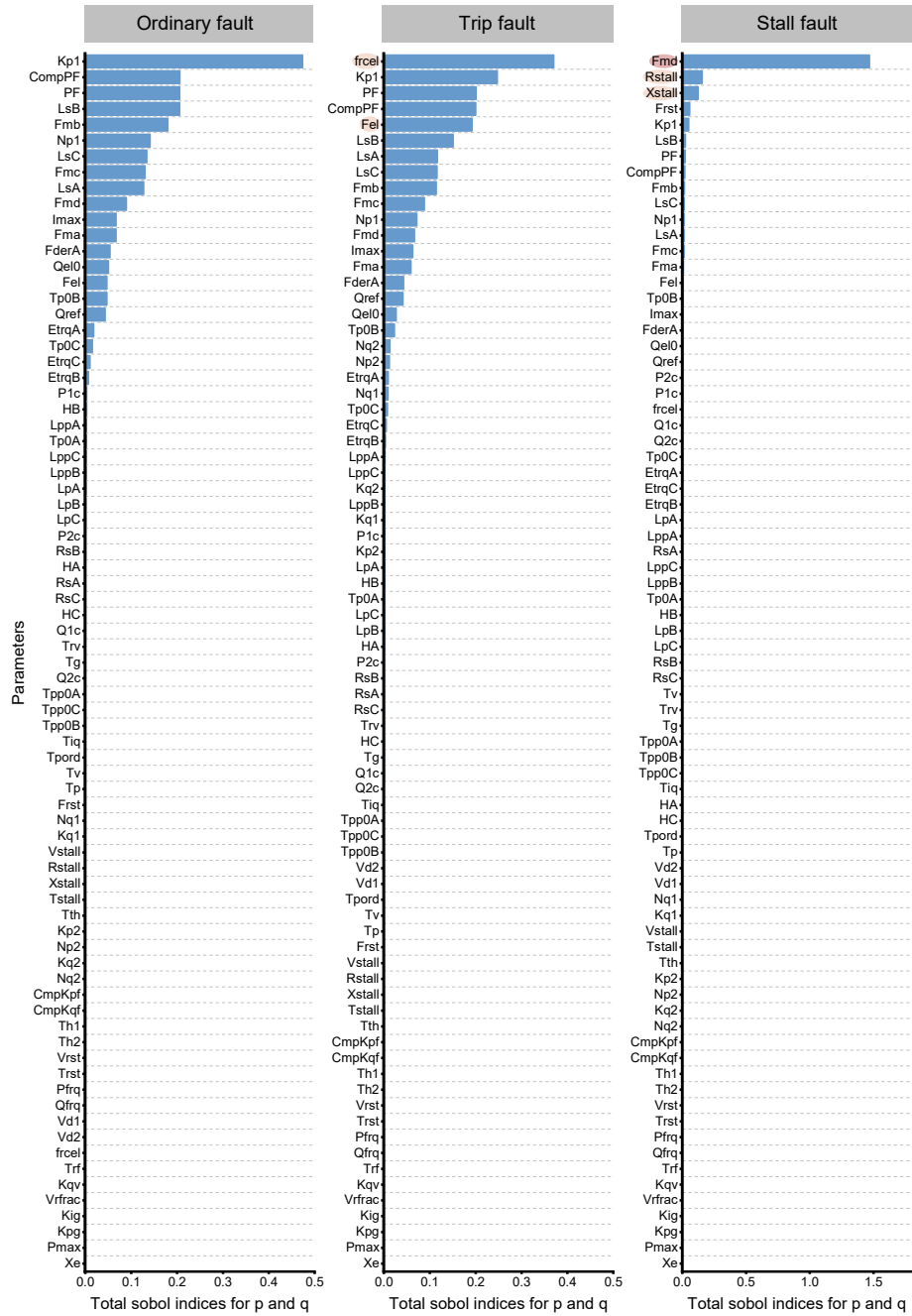
become much more sensitive when there are power electronic loads tripping. With the occurrence of motor D stalling, F_{md} emerges as the most sensitive parameter, exhibiting significantly higher sensitivity compared to other parameters. Additionally, the sensitivities of R_{stall} , X_{stall} , and F_{rst} increase markedly. Comprehensively considering the sensitivity rankings under the three fault events, 30 sensitive parameters are selected for parameter estimation. They are listed in Supplementary Table 2.

Supplementary Table. 2 List of selected model parameters for identification

Notations	Description	Sampling ranges	Default values
F_{ma}	Motor A fraction	[0.1,0.3]	0.2
F_{mb}	Motor B fraction	[0.1,0.3]	0.2
F_{mc}	Motor C fraction	[0.1,0.3]	0.2
F_{md}	Motor D fraction	[0.1,0.3]	0.2
F_{el}	Electronic load fraction	[0.1,0.3]	0.2
F_{derA}	DER_A fraction	[-0.3,-0.1]	-0.2
L_{sA}	Synchronous reactance (pu) of motor A	[1.5,3]	1.8
E_{trqA}	Speed exponent for mechanical torque of motor A	[0,1]	0
L_{sB}	Synchronous reactance (pu) of motor B	[1.5,3]	1.8
T_{p0B}	Transient open circuit time constant (sec.) of motor B	[0.08,0.12]	0.1
E_{trqB}	Speed exponent for mechanical torque of motor B	[1.5,2.5]	2
L_{sC}	Synchronous reactance (pu) of motor C	[1.5,3]	1.8
T_{p0C}	Transient open circuit time constant (sec.) of motor C	[0.08,0.12]	0.1
E_{trqC}	Speed exponent for mechanical torque of motor C	[1.5,2.5]	2
R_{stall}	Stall resistance (pu) of motor D	[0.08,0.12]	0.1
X_{stall}	Stall reactance (pu) of motor D	[0.08,0.12]	0.1
$CompPF$	Power factor of motor D	[0.9,1]	0.98
F_{rst}	Fraction of load that can restart after stalling of motor D	[0.15,0.3]	0.2
K_{p1}	Active power coefficient of motor D in run state	[-1,1]	0
N_{p1}	Active power exponent of motor D in run state	[0.5,1.5]	1
N_{q1}	Reactive power exponent of motor D in run state	[1,3]	2
N_{p2}	Active power exponent of motor D in stall state	[1.6,4.8]	3.2
N_{q2}	Reactive power exponent of motor D in stall state	[1.25,3.75]	2.5
P_{1c}	Coefficient of P_1 for static load	[0.3,0.5]	0.4
P_{2c}	Coefficient of P_2 for static load	[0.5,0.7]	0.6
PF	Power factor of static load	[0.9,1]	0.95
f_{rcel}	Fraction of electronic load that recovers from low voltage trip	[0.5,0.9]	0.75
Q_{el0}	Initial reactive power of power electronic load	[0.1,0.3]	0.2
I_{max}	Maximum current of DER_A (pu)	[1,1.5]	1.2
Q_{ref}	Reactive power reference of DER_A (pu)	[0.1,0.3]	0.2



Supplementary Fig. 5 Sobol's indices of model parameters. The Sobol indices of model parameters in CMLPDWG are calculated for both active and reactive power trajectories under different fault events. The bars in light blue and dark blue correspondingly represent the first-order and total-effect indices: (left) ordinary fault, (middle) trip fault, and (right) stall fault.



Supplementary Fig. 6 The rankings of parameter sensitivity under different fault events. The model parameters in Cmpldwg are ranked according to the total-effect indices for both active and reactive power trajectories: **(left)** ordinary fault, **(middle)** trip fault, and **(right)** stall fault.

4 Supplementary information of JCDI

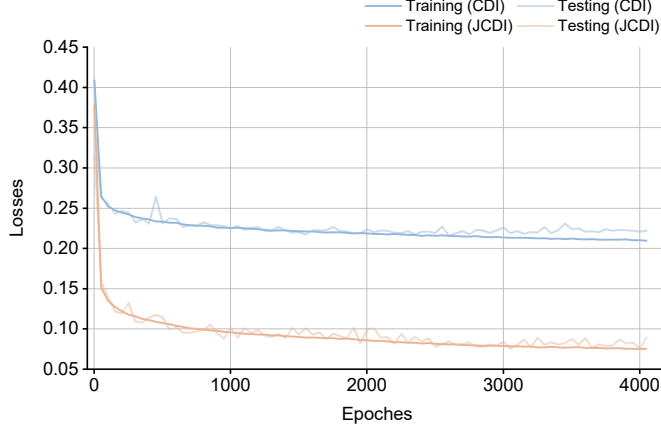
Data generation. We randomly sample the sensitive model parameters from a uniform distribution within the ranges specified in Supplementary Table 2. Then, dynamic simulations described in Supplementary Section 2 are performed using these parameters in CMPLDWG to obtain the dynamic responses. The sampling ranges are determined by considering both physical constraints of electric parameters (such as L_{sA}) and perturbations of up to 50% to the settable parameters (such as F_{ma}). The total dataset size is 300000, including 250000 data samples for training and 50000 for testing.

Training details. The hyperparameters for JCDI are listed in Supplementary Table 3. The trajectory encoder employs a ResNet architecture. It encodes power trajectories using a stem layer (kernel size 4, stride 4, 32 kernels) followed by two pairs consisting of a residual block and a downsampling layer. Each downsampling layer has a stride of 4 and a kernel size of 4, containing 128 and 256 convolutional kernels, respectively. This architecture transforms the input power trajectory of shape (2, 512) into a latent representation of shape (256, 8). The transformer encoder is composed of three layers, each containing a multi-head attention mechanism with four attention heads. For the diffusion process, the diffusion step is 200, and a linear variance schedule is used to add noise. The Adam optimizer is used to minimize the loss function with a learning rate of 1×10^{-4} and a batch size of 128. Training is implemented with PyTorch on a NVIDIA GeForce RTX 3090 graphics processing unit (GPU).

Supplementary Table. 3 Hyperparameters for JCDI

Parameter types	Hyperparameters	Notations	Values
Diffusion model	Diffusion step	T	200
	Initial value of variance schedule	β_0	0.0001
	Final value of variance schedule	β_T	0.005
Training	Batch size	B	128
	Learning rate	lr	1×10^{-4}
Trajectory encoder	Stem layer (kernel size, number)	-	[1 × 4, 32]
	Downsampling layer 1	-	[1 × 4, 128]
	Downsampling layer 2	-	[1 × 4, 256]
Transformer encoder	Number of layers	-	3
	Number of heads	-	4
	Features in the input	-	256
	Features in the feed-forward network	-	512

Training progress. Supplementary Fig. 7 shows the evolution of training and testing losses in the training progress. As the number of epochs increases, they both decrease smoothly and level off at similar values, demonstrating that the models are not overfitting to the training data. It is also important to note that the losses for JCDI are significantly lower than those for CDI.



Supplementary Fig. 7 Loss evolution in the training progress. The dark and light blue lines respectively represent the training and testing losses for CDI, while the orange lines are those for JCDI.

Posterior results. Supplementary Figure 8 presents the complete posterior results of parameter estimation.

5 Supplementary information of comparative algorithms

Reinforcement learning. We formulate the parameter calibration process for CMPLDWG as a Markov decision process (MDP). The agent starts from an initial parameter estimation state, modifying the parameters at each step. Then, it transfers to the next state of estimation and obtains a reward signal in this transition. Through this process, the agent learns a policy capable of adjusting model parameters to minimize observation error. The state is defined as the current estimation of parameters as expressed by (Supplementary Equation 3).

$$s = \hat{\theta}. \quad (\text{Supplementary Equation 3})$$

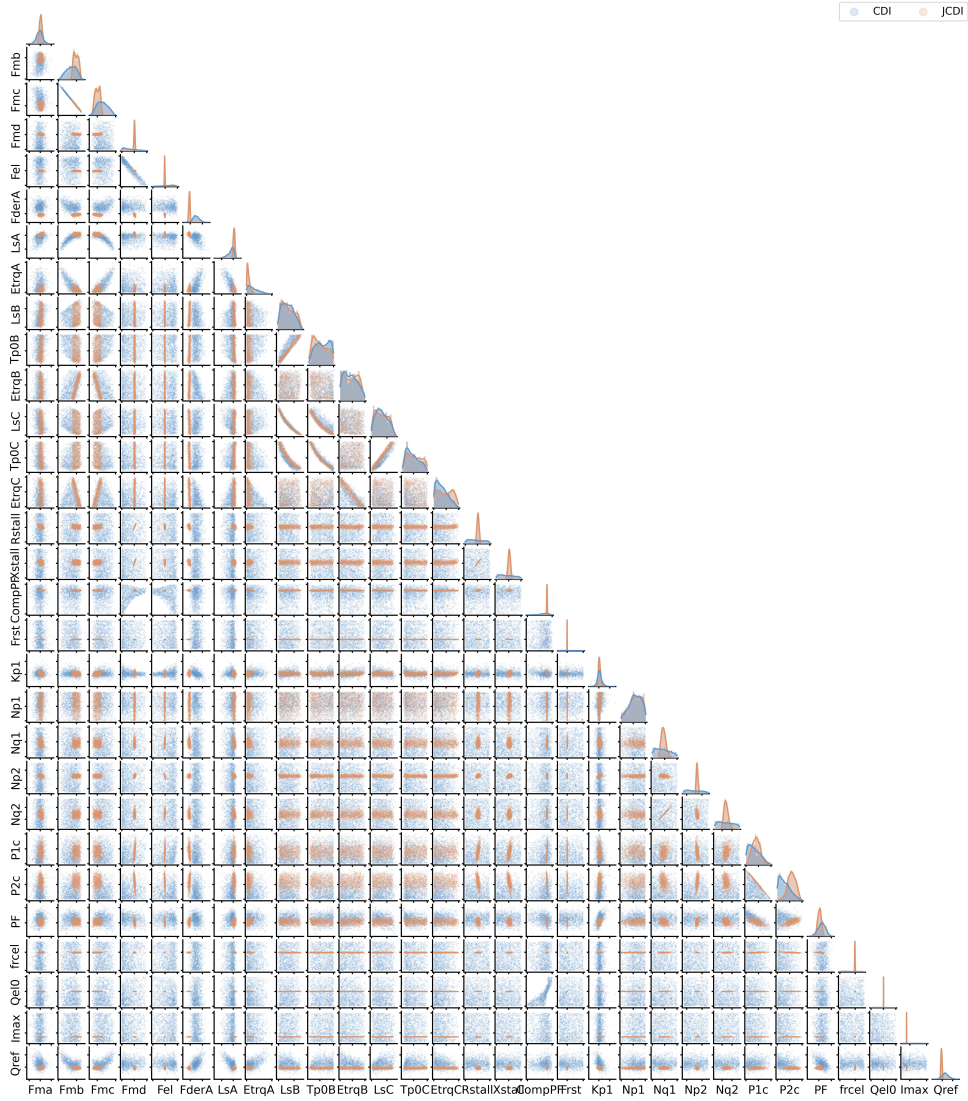
Action is defined as the adjustment of parameters, which is expressed by (Supplementary Equation 4).

$$a = \Delta\hat{\theta}. \quad (\text{Supplementary Equation 4})$$

State transition represents the parameter update as shown in (Supplementary Equation 5).

$$s' = \hat{\theta}' = \hat{\theta} + \Delta\hat{\theta}. \quad (\text{Supplementary Equation 5})$$

Reward is calculated based on the change in root mean squared error (RMSE) of dynamic power responses (formulated in equation (3)). To motivate continuous accuracy



Supplementary Fig. 8 Posterior results of parameter estimation. The subplots in the lower triangular region display the scatter plots of parameter estimates. Marginal posterior distributions for each model parameter are plotted along the diagonal. Blue plots represent CDI results, while orange plots show JCDI results.

improvement when RMSE is small, a reciprocal representation is used, as shown in (Supplementary Equation 6).

$$r = -\Delta \frac{1}{RMSE+0.1}. \quad (\text{Supplementary Equation 6})$$

We use deep Q-learning (DQN) to solve the parameterization problem [14]. DQN is a value-based reinforcement learning method that updates the action-value function (Q function) by the temporal difference approach as expressed by (Supplementary Equation 7). In this work, the Q function is approximated by a fully connected neural network, including two hidden layers with 512 and 256 units, respectively. The ε -greedy policy with a piecewise exploration schedule is used to realize the trade-off between exploration and exploitation. The training parameters for DQN are listed in Supplementary Table 4.

$$Q(s', a) = Q(s, a) + \alpha \cdot (r' + \gamma \cdot \max_a Q(s', a) - Q(s, a)),$$

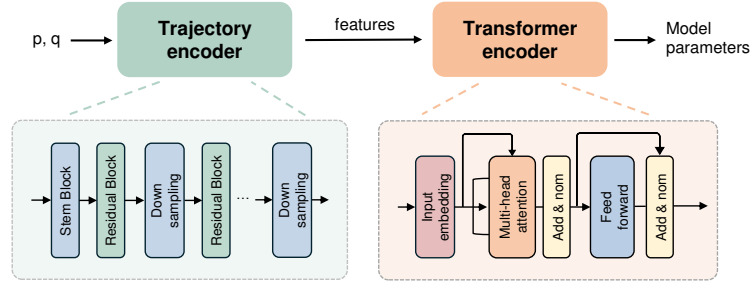
(Supplementary Equation 7)

where $Q(s, a)$ denotes the action-value function, α represents the learning rate, and γ is the discount factor.

Supplementary Table. 4 Hyperparameters for DQN

Hyperparameters	Notations	Values
Batch size	B	32
Learning rate	α	Decay from 1×10^{-3} to 5×10^{-5}
Replay buffer size	B_r	5000
Target update frequency	f_T	500
Exploration	ε	Decay from 1 to 0.01
Discount rate	γ	0.99

Supervised learning. Supplementary Figure 9 illustrates the neural network structure for supervised learning (SL). A ResNet-based trajectory encoder (Res-TFR) extracts features from active and reactive power trajectories. These features are then tokenized and processed by a transformer encoder to infer the model parameters. Supplementary Table 5 lists the algorithm parameters.



Supplementary Fig. 9 The neural network structure for SL. The neural network for SL, Res-TFR, consists of a ResNet-based trajectory encoder in series with a transformer encoder. It learns the mapping between power trajectories and model parameters.

Supplementary Table. 5 Hyperparameters for SL

Parameter types	Hyperparameters	Notations	Values
Training	Batch size	B	128
	Learning rate	lr	1×10^{-4}
Trajectory encoder	Stem layer (kernel size, number)	-	$[1 \times 4, 32]$
	Downsampling layer 1	-	$[1 \times 4, 128]$
	Downsampling layer 2	-	$[1 \times 4, 256]$
Transformer encoder	Number of layers	-	3
	Number of heads	-	4
	Features in the input	-	256
	Features in the feed-forward network	-	512

References

- [1] WECC composite load model with DG specification. Technical report, Western Electricity Coordinating Council (WECC) (2015)
- [2] WECC composite load model specification technical report. Technical report, Western Electricity Coordinating Council (WECC) (2021)
- [3] Technical reference on the composite load model. Technical report, The Electric Power Research Institute (EPRI) (2020)
- [4] Ma, Z., Wang, Z., Wang, Y., Diao, R., Shi, D.: Mathematical representation of WECC composite load model. *Journal of Modern Power Systems and Clean Energy* **8**(5), 1015–1023 (2020)
- [5] The new aggregated distributed energy resources (der_a) model for transmission planning studies: 2019 update. Technical report, Electric Power Research Institute (2019)
- [6] OPAL-RT TECHNOLOGIES, Inc.: ePHASORSIM User Document. <https://opal-rt.atlassian.net/wiki/spaces/PEUD/pages/144472811/Positive+Sequence+Fault> (2024)
- [7] Kundur, P.: *Power System Stability and Control*. McGraw-Hill, New York (1994)
- [8] Xinzhou, D., Bing, W., Shi, S.: *Modern Power System Protection*. Tsinghua University Press, Beijing (2023)
- [9] Sobol, I.M.: Global sensitivity indices for nonlinear mathematical models and their monte carlo estimates. *Mathematics and Computers in Simulation* **55**(1), 271–280 (2001) [https://doi.org/10.1016/S0378-4754\(00\)00270-6](https://doi.org/10.1016/S0378-4754(00)00270-6) . The Second IMACS Seminar on Monte Carlo Methods
- [10] Tosin, M., Côrtes, A.M., Cunha, A.: A tutorial on sobol’global sensitivity analysis applied to biological models. *Networks in Systems Biology: Applications for Disease*

Modeling, 93–118 (2020)

- [11] Saltelli, A.: Making best use of model evaluations to compute sensitivity indices. *Computer Physics Communications* **145**(2), 280–297 (2002) [https://doi.org/10.1016/S0010-4655\(02\)00280-1](https://doi.org/10.1016/S0010-4655(02)00280-1)
- [12] Iwanaga, T., Usher, W., Herman, J.: Toward SALib 2.0: Advancing the accessibility and interpretability of global sensitivity analyses. *Socio-Environmental Systems Modelling* **4**, 18155 (2022) <https://doi.org/10.18174/sesmo.18155>
- [13] Herman, J., Usher, W.: SALib: An open-source python library for sensitivity analysis. *The Journal of Open Source Software* **2**(9) (2017) <https://doi.org/10.21105/joss.00097>
- [14] Mnih, V., Kavukcuoglu, K., Silver, D., Rusu, A.A., Veness, J., Bellemare, M.G., Graves, A., Riedmiller, M., Fidjeland, A.K., Ostrovski, G., *et al.*: Human-level control through deep reinforcement learning. *nature* **518**(7540), 529–533 (2015)